DOI: 10.15480/882.9330

Eighth International Symposium on Marine Propulsors
smp'24, Berlin, Germany, March 2024

Model- and Full-Scale Tip-Raked Marine Propellers: Analysis of the Scale Effects in Open Water Conditions

Ginevra Rubino, Moustafa Abdel-Maksoud

Institute for Fluid Dynamics and Ship Theory, Hamburg University of Technology, Hamburg, Germany

ABSTRACT

This paper proposes the numerical investigation of the scale effects in open water for two tip-raked marine propellers. The turbulence model $k-\omega$ SST is applied for full-scale simulations, while the transition model $\gamma - Re_\theta$ is used in model-scale. The hydrodynamic performance at different loading conditions is analyzed, and predictions indicate small Reynolds number effects for these two unconventional propellers. Whereas the predicted propeller efficiency is within a 2% relative deviation from measurements in model-scale, efficiency predictions in full-scale quantitatively deviate from the extrapolated-to-full-scale values, particularly at high advance ratios. Skin friction distributions and limiting streamlines at model-, with and without transition model, and full-scale are analyzed at the design conditions. It is concluded that the negligible predicted scale effects are related to the considerably dissimilar boundary layer flows at different Reynolds numbers and to the vortex shedding behind the blunt trailing edge for one of the two propellers. Finally, it is noted that $k-\omega$ SST predicts more significant scale effects than $\gamma - Re_\theta$ when also used to compute model-scale results. This behavior emphasizes the importance of using a transition model for low-Reynolds number flows.

Keywords

Tip-Raked Marine Propellers, Scale Effects, Transition Models

1 INTRODUCTION

Full-scale propeller performance is typically extrapolated analytically or statistically from open water model-scale experimental results. This approach is dictated by the size and speed limitations for the experimental set-up in towing tanks or cavitation tunnels, for which Reynolds number (Re) similarity conditions cannot be met. The measured hydrodynamic characteristics of the open water tests are usually corrected to full-scale using rather simple extrapolation methods. An overview of the different methods can be found in Helma et al. (2017). Among these, the most commonly used is the 1978 ITTC procedure (ITTC 1978). It is based on the Lerbs assumption that a propeller can be represented by a characteristic section at either 70% or 75% of its radius. Thus, full-scale performance characteristics are obtained by taking into account the change in drag coefficient at the blade section due to the different flow regimes at different Re. This procedure was proven to be acceptable for conventional propellers, but may fail for unconventional, new-generation, and highly performing propellers, that often present skewed and tip-raked designs. In addition, the full-scale corrections may not be enough to reflect the different flow regimes at the different Re.

Scale effects are viscous in nature and are related to boundary layer phenomena. While at full-scale the boundary layer can be assumed to be fully turbulent, at model-scale flow transition plays an important role and needs to be accounted for to predict correctly the propeller performance. To clarify the scaling problem, the ITTC committee (2014,2017) has encouraged the scientific community to use Computational Fluid Dynamics (CFD) tools to have a deeper insight into the flow physics at different Reynolds number regimes. Given the advance in high-performance computing Reynolds-Averaged Navier-Stokes (RANS) solvers and the development of new CFD models in the last two decades, an accurate flow simulation in model-scale, which accounts for laminar-to-turbulence transition, is possible.

Nowadays, transition models have been progressively introduced in RANS computations to better analyze the propeller performance. First calculations using the local correlation transition model (LCTM) $\gamma - Re_\theta$ were presented by Müller et al. (2009), using ANSYS-CFX. Bhattacharyya et al. (2016) and Pawar et al. (2019) applied $\gamma - Re_\theta$ to ducted propellers, and Gaggero (2020) tested STAR-CCM+ and OpenFOAM $\gamma - Re_\theta$ implementations on a conventional and a CLT (Contracted Loaded Tip) propeller. Moran-Guerrero et al. (2018) investigated the influence of crossflow effects on the open water predictions on two conventional and one CLT propellers in STAR-CCM+.

Transition models are also employed in the investigation of scale effects. Their use aims to achieve a more reliable estimation of Re effects, which would not be possible without consideration of flow transition. Shin & Andersen

(2017) studied the performance in model- and full-scale of both a conventional and a tip-modified propeller. They concluded that scale effects are more important on the tip-modified propeller, because of a larger increase in K_T from model- to full-scale due to a weaker separation in the latter case. Yao & Zhang (2018) investigated the scale effects on the VP1304 conventional propeller. They analyzed the *Re* effects in terms of thrust and torque coefficients, pressure and skin friction distributions, and tip vortex strength variation. Their results showed that scale effects are minimized past a critical *Re* value. Finally, Baltazar et al. (2021) analyzed the performance of the four-bladed conventional marine propeller S6368 at different Reynolds numbers. They observed that at the design operation point, the thrust coefficient increases with *Re*, while smaller variations of the torque coefficient are achieved.

Within this context, the objective of this study is to provide additional insight into the scale effects for tip-raked propellers. The latter have known growing recognition during the last years as possible solutions to reduce fuel consumption and greenhouse gas emissions in maritime operations because of their higher propulsive efficiency. The presented work focuses on the evaluation of the scale effects on two propellers, hereafter referred to as P3590 and P1951. The geometries were designed at the Hamburg Ship Model Basin (HSVA), and the Schiffbau-Versuchsanstalt Potsdam (SVA), respectively. The flow around the two propellers is simulated at two different Reynolds numbers in open water conditions. Experimental data from HSVA and SVA, provided within the 'Design of Efficient Ship Propellers with Unconventional Form' (DeffProForm)[*] collaborative project, are used to validate transition front predictions in model scale. Full-scale performance predictions (thrust and torque coefficients) are further compared to full-scale extrapolated values obtained using the 1978 ITTC procedure for the P1951 and Streckwall's strip method (Streckwall et al. 2013) for the P3590. The latter is an extrapolation method based on friction lines statistically extracted from CFD predictions on different propellers. A local skin friction coefficient is used to compute the sectional drag by integrating the laminar and turbulent parts of the skin friction contribution. It is worth mentioning that the two extrapolation-to-full-scale methods, Streckwall's strip method for HSVA and ITTC 1978 for SVA, were selected by each institute, based on their established practices. The computed extrapolated values were then shared with the authors within the collaborative project.

This paper is organized as follows: the mathematical models, including the turbulence and transition models, are given in Section 2. Section 3 is devoted to the description of the propellers' geometry, flow solver, and the numerical set-up. The results are presented and discussed in Section 4, and the main conclusions of this study are given in Section 5.

2 MATHEMATICAL MODEL

2.1 RANS Equations

Flow predictions are based on the resolution of the RANS equations. In the presented analysis, two different reference systems are considered: an earth-fixed reference system (X,Y,Z), where the components of the absolute velocity are u_i, and a non-inertial propeller-fixed reference frame (x,y,z), rotating with constant angular velocity ω. The velocity components in the latter reference frame are v_i and they are commonly referred to as relative velocity. Since the propellers are performing in open water conditions, the flow is statistically steady in the non-inertial rotating frame. Given an incompressible flow, the RANS continuity and momentum equations in the (x,y,z) reference system, considering the absolute velocity components u_i as unknowns, can be written as:

$$\frac{\partial u_i}{\partial x_i} = 0, \tag{1}$$

$$\rho v_j \frac{\partial u_i}{\partial x_j} + \rho \varepsilon_{ijk} \omega_i u_k = -\frac{\partial p}{\partial x_i} + (\mu + \mu_t) \frac{\partial}{\partial x_j} \left(\frac{\partial u_i}{\partial x_j} + \frac{\partial u_j}{\partial x_i} \right), \tag{2}$$

where ρ is the fluid density, μ the dynamic fluid viscosity and μ_t is the eddy dynamic viscosity, and ε_{ijk} is the Levi-Civita symbol.

2.2 $k-\omega$ SST Turbulence Model

The $k-\omega$ Shear Stress Transport (SST) two equations eddy-viscosity model developed by Menter et al. (1994) is a blend between $k-\omega$ and $k-\varepsilon$ formulations. The $k-\varepsilon$ formulation is used in the free-stream, to avoid the dependence of $k-\omega$ on the free-stream turbulence intensity. Then, the model switches to the $k-\omega$ formulation in the boundary layer, because of its superior behavior within the viscous sub-layer. The steady transport equations for the two turbulence variables k and ω are:

$$\rho u_i \frac{\partial k}{\partial x_i} = P_k - D_k + (\mu + \sigma_k \mu_t) \frac{\partial}{\partial x_i} \left(\frac{\partial k}{\partial x_i} \right), \tag{3}$$

$$\rho u_i \frac{\partial \omega}{\partial x_i} = P_\omega - D_\omega + (\mu + \sigma_\omega \mu_t) \frac{\partial}{\partial x_i} \left(\frac{\partial \omega}{\partial x_i} \right) + CD_\omega. \tag{4}$$

P_k and P_ω are the respective production terms, while $D_k = \beta^* k\omega$ and $D_\omega = \beta\omega^2$ are the destruction terms. The term CD_ω is the so-called cross diffusion term, which results from the derivation of the ω equation from the the turbulence dissipation, ε, equation. Details on the constants σ_k, σ_ω, β and β^*, as well as the exact terms, can be found in the original publication.

2.3 $\gamma - Re_\theta$ Transition Model

The two equations $\gamma - Re_\theta$ transition model was proposed by Langtry (2006) within the LCTM framework. The intermittency γ transport equation is:

$$\rho u_i \frac{\partial \gamma}{\partial x_i} = P_\gamma - D_\gamma + \frac{\partial}{\partial x_i} \left[\left(\mu + \frac{\mu_t}{\sigma_\gamma} \right) \frac{\partial \gamma}{\partial x_i} \right], \tag{5}$$

where P_γ and D_γ are the production and destruction terms, respectively, and σ_γ is a constant. The second equation for

[*] Accessed on October 2023: https://www.tuhh.de/panmare/applications/research-projects/current-projects/deffproform

the local transition momentum thickness Reynolds number $\overline{Re_{\theta_t}}$ reads as:

$$\rho u_i \frac{\partial \overline{Re_{\theta_t}}}{\partial x_i} = P_{\theta_t} + \frac{\partial}{\partial x_i}\left[\sigma_{\theta_t}\left(\mu + \mu_t\right)\frac{\partial \overline{Re_{\theta_t}}}{\partial x_i}\right]. \quad (6)$$

Eq.(6) has only the production term P_{θ_t}, which is based on empirical correlations and is active outside the boundary layer. σ_{θ_t} is a constant. The coupling between the transition and turbulence model acts on the turbulence kinetic energy k equation, Eq.(3), and on the function that controls the switch between $k-\omega$ and $k-\varepsilon$ formulations. The equation for ω, Eq.(4), remains invariant. This transition model, as originally published, accounts for two-dimensional transition mechanisms, such as Tolmienn-Schlichting waves and bypass. Modifications of the production terms are needed to include crossflow transition.

3 PROBLEM OVERVIEW AND SET-UP

3.1 Propeller Geometries

The two five-bladed unconventional propeller geometries, the P3590 and P1951, are shown in Fig. 1. They are both labeled as unconventional designs, because of their tip raked towards the suction and pressure side, respectively.

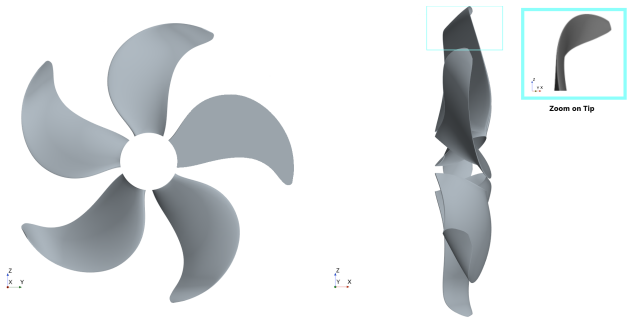

(a) P3590: Front view. (b) P3590: Side view.

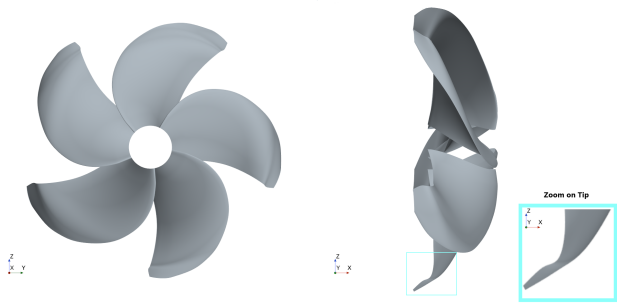

(c) P1951: Front view. (d) P1951: Side view.

Figure 1: P1951 and P3590: front and side views of the geometries and zooms on the raked tip.

The propellers' main geometrical features are listed in Table 1. Two set of experiments were carried out: one at HSVA, for the P3590, and one at SVA Potsdam, for the P1951, in their respective towing tanks. The measurements include thrust and torque coefficients at different loading conditions and rotational speeds, as well as paint tests at specific operating conditions.

3.2 Solver

The simulations presented in the paper are carried out using the unstructured finite volume solver STAR-CCM+ version 17.06.007, developed by Siemens. It is a finite volume solver, based on variables collocated in the cell centers and a face-based implementation that allows for arbitrary cell shapes and unstructured meshes.

Table 1: Overview of the propellers' main particulars in model-scale. The subscript $_{0.75R}$ indicates that the geometrical features are calculated at the radius $r = 0.75R$, where R is the propeller's radius.

	P3590	P1951
Diameter D $[mm]$	250.00	230.00
Chord ratio $C_{0.75R}/D$	0.27	0.29
Pitch ratio $P_{0.75R}/D$	1.0824	0.99250
Blade-area ratio A_E/A_0	0.6033	0.843620
Number of blades	5	5
Scale factor	38	9.1304

Predictions are obtained using a segregated method that employs a SIMPLE approach for the pressure-velocity coupling. Transition is modeled with the LCTM model $\gamma - Re_\theta$. Crossflow transition is not accounted for in the present analysis, as it is not expected to play an important role for the Reynolds numbers considered in this study. $\gamma - Re_\theta$ is coupled to the $k-\omega$ SST turbulence model for the resolution of the turbulence variables. The Durbin limiter is set by default to control the production of turbulence kinetic energy at the stagnation point.

3.3 Computational Domain and Boundary Conditions

The computational domain, presented in Fig. 2, exploits the periodicity of the propeller geometry, thus a single blade with the front hub-cap and downstream shaft is modeled setting to periodic conditions on the sides. The flow is solved in steady-state using a moving reference frame approach.

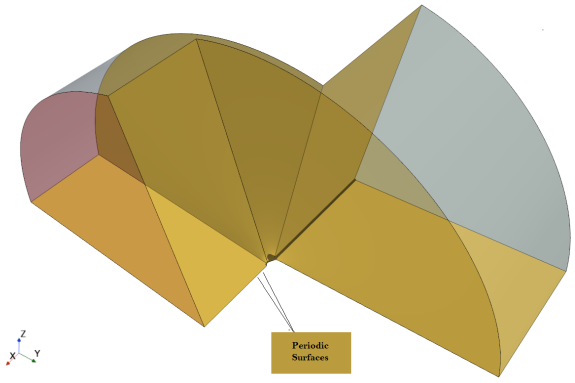

Figure 2: Periodic Mesh. Periodic surfaces are colored in yellow, while the outer surfaces in gray.

The inlet is positioned four propeller's diameters ahead of the propeller plane, while the outlet six propeller's

diameter behind. The diameter of the one-fifth cylindrical domain is ten times the propeller's diameter. Velocity, transition quantities, and turbulence intensity and eddy viscosity ratio are specified at the inlet. Further details on the inlet boundary conditions are given in Sec.(4). The outer surfaces are treated with slip conditions, while zero-gradient boundary condition is imposed at the outlet. Uniform flow is prescribed as initial solution.

3.4 Grid Set

Simulations at model-scale are run on a set of six unstructured polyhedral grids generated using STAR-CCM+ mesh generator. For the mesh generation, several subdomains are set to control the overall mesh size. The latter depends on the propeller's diameter D, which is divided by multiples of $\sqrt{2}$ during the mesh convergence study. The subdomains include the thickness of the first cell at the wall, as well as the boundary layer thickness itself. The boundary layer growth factor, $r = 1.2$, and the number of prism layers, $N_{layers} = 30$ for P3590, $N_{layers} = 32$ for P1951, are fixed in the mesh convergence study. For the surface mesh, the target mesh size is uniformly set to 1.5% of the base size, while the leading and trailing edges, defined as feature curves, have a target mesh size equal to 0.15% of the base size. An overview of the grids, number of cells in the volume, N_V, and in the surface mesh, N_S, and the predicted averaged dimensionless wall distance of the first cell height at the blade surface, y^+_{avg}, are given in Table 2 for P3590 and in Table 3 for P1951. The y^+_{avg} values correspond to the calculations by $\gamma - Re_\theta$ at the propellers' respective design condition and in model-scale. Except for local maxima y^+ values at the leading edge on the suction side over 1, $y^+ < 1$ and the boundary layer is fully resolved in model-scale. The two quantities considered in the mesh convergence study are the thrust, $K_T = T/(\rho n^2 D^4)$, and the torque coefficients, $10K_Q = 10Q/(\rho n^2 D^5)$, where T and Q are the thrust and torque, respectively, and n $[Hz]$ is the propeller rotation rate. The convergence of K_T and $10K_Q$, as predicted by $\gamma - Re_\theta$ in model-scale, with respect to the relative step size h_i/h_1, with $h_i = (1/N_V)^{(1/3)}$, is presented in Fig. 3. The plots also show the numerical uncertainties as obtained following the procedure for the estimation of the discretization error by Eça and Hoekstra (2014). The apparent convergence order of both quantities for the P3590 shows the expected 2nd-order convergence behavior over mesh refinement, while the results for P1951 show a quasi-1st-order convergence. For the latter propeller, the last two grids are not considered for the fit, since they are outside the asymptotic range. In both cases, the results do not converge monotonically. This behavior is expected since it is due to the use of unstructured grids. The estimated uncertainties, which depend on the observed order of accuracy and the standard deviation of the fit, are of the order 0.4%-4.5%, being higher for P1951. In general, higher quality meshes could reduce numerical uncertainty and improve the results' convergence over mesh refinement.

The relative difference of the thrust and torque coefficients to the finest grid are reported in Table 2 and Table 3 for P3590 and P1951, respectively. For the simulations presented in the following, it is opted to use Grid 3 for P3590 and Grid 2 for P1951 (colored in red in their respective table). The grid for each propeller is chosen based on the relative difference of the torque and thrust coefficients to the measurements and the results on the finest grid, in addition to practical purposes. Grid 2 for P1951 and Grid 3 for P3590 are considered fine enough to provide accurate predictions in terms of thrust and torque coefficients and transition front, as identified through the wall streamlines. Finally, a finer mesh is chosen for P1951, because it is observed that an accurate resolution of the pressure gradient on the concave suction side requires additional cells at the surface.

Since the results of the mesh convergence study performed at model-scale are considered to be valid also for the full-scale case, only the model-scale mesh selected for each propeller is scaled to full dimensions. Specifically, the base size is multiplied by the scale factor, and the constraints on the surface and volume mesh refinement are kept the same. The thickness of the first cell at the wall and the boundary layer thickness are set independently of the scale factor, as they do not vary linearly with it. To assess the effect of the wall treatment in full-scale, two meshes for each propeller are created with the same surface and volumetric refinements, boundary layer thickness, but different thicknesses of the first cell at the wall and number of prism layers. For the 'wall-function' meshes, the thickness of the first cell at the wall is set to assure the predicted y^+ to be bigger than 30. The target y^+ is estimated based on the formula proposed by Choi &

Table 2: P3590: Variation of the thrust and torque coefficients with respect to the results obtained on the finest grid, Grid 1, at $J = 0.788$. N_V indicates the number of cells in the volume, while N_S on the one-blade surface. M denotes millions. The relative deviation is defined as $E(\%) = (\phi_1 - \phi)/\phi_1$, with ϕ_1 solution on Grid 1.

	N_V	N_S	y^+_{avg}	$\Delta K_T(\%)$	$\Delta K_Q(\%)$	$\Delta\eta(\%)$
Grid 1	32.0M	1.66M	0.12	–	–	–
Grid 2	21.0M	1.06M	0.17	−0.1%	−0.2%	0.1%
Grid 3	12.2M	619 000	0.24	−0.03%	−0.32%	0.29%
Grid 4	8.2M	409 000	0.34	0.41%	−0.13%	0.54%
Grid 5	5.4M	254 000	0.5	1.4%	0.55%	0.86%
Grid 6	3.8M	169 000	0.69	1.25%	0.02%	1.23%

Table 3: P1951: Variation of the thrust and torque coefficients with respect to the results obtained on the finest grid, Grid 1, at $J = 0.6$. N_V indicates the number of cells in the volume, while N_S on the one-blade surface. M denotes millions. The relative deviation is defined as $E(\%) = (\phi_1 - \phi)/\phi_1$, with ϕ_1 solution on Grid 1.

	N_V	N_S	y^+_{avg}	$\Delta K_T(\%)$	$\Delta K_Q(\%)$	$\Delta\eta(\%)$
Grid 1	$39.1M$	$1.88M$	0.15	–	–	–
Grid 2	$22.1M$	$1.06M$	0.21	0.33%	0.42%	−0.09%
Grid 3	$14.0M$	677000	0.3	0.49%	0.6%	−0.11%
Grid 4	$8.8M$	414000	0.42	0.82%	0.98%	−0.16%
Grid 5	$5.9M$	270000	0.59	0.69%	0.91%	−0.22%
Grid 6	$3.9M$	172000	0.84	0.62%	0.6%	0.02%

Kim (2020). The number of prism layers in the boundary layer are set to $N_{layers} = 18$ for P3590 and $N_{layers} = 14$ for P1951, and the boundary layer growth factor is kept equal to $r = 1.2$. The meshes in full-scale using wall functions count a total of $11M$ cells, of which $1M$ on the blade surface, for the P1951, and $7.8M$, of which 314 000 on the blade surface, for the P3590.

For the 'wall-resolved' meshes, the thickness of the first cell at the wall is reduced to obtain an average $y^+ < 1$ on the blade. The number of prism layers is then increased to $N_{layers} = 45$ for P3590, $N_{layers} = 41$ for P1951. The 'wall-resolved' mesh for the P3590 counts approximately $16M$ cells with a predicted $y^+_{avg} = 0.69$, while $26M$ cells with a predicted $y^+_{avg} = 0.58$ for the P1951.

The predicted y^+_{avg} values are higher than those computed on their 'similar' grids in model-scale. Indeed, similar values of y^+_{avg} as in model-scale would require meshes with a first cell at the wall of thickness of the order of 10^{-7}.

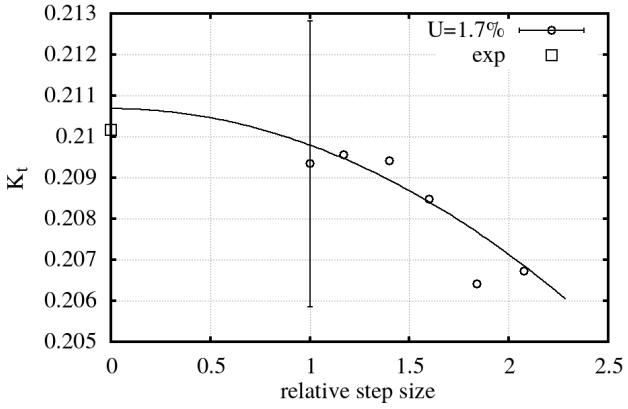

(a) P3590: K_T.

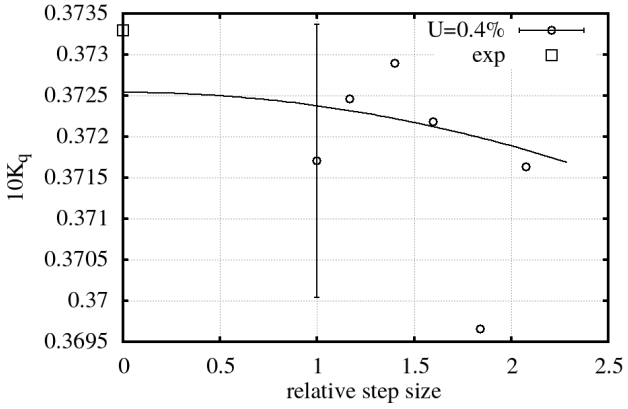

(b) P3590: $10K_Q$.

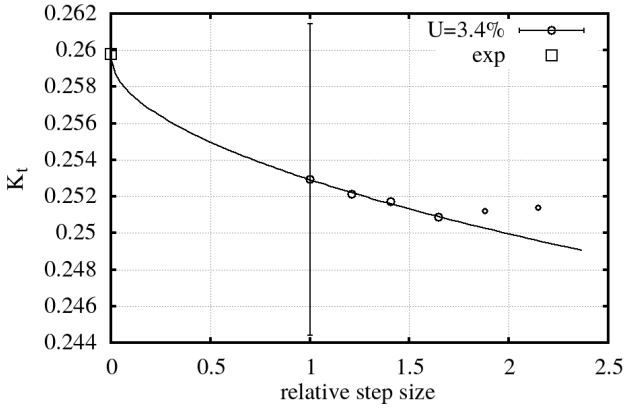

(c) P1951: K_T .

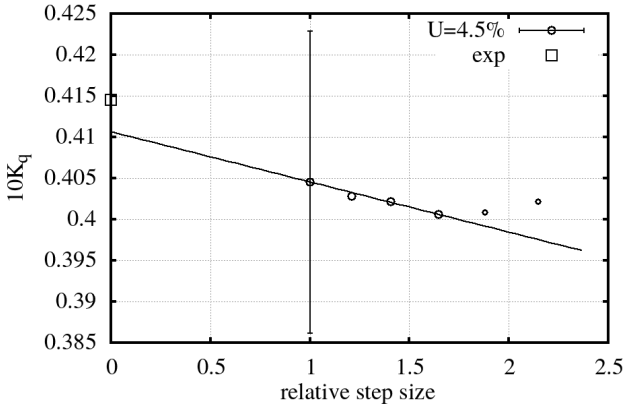

(d) P1951: $10K_Q$.

Figure 3: P3590 and P1951: K_T and $10K_Q$ mesh convergence study. Uncertainties are computed using the numerical analysis uncertainty tool developed at MARIN institute. Accessed on October 2023: https://www.marin.nl/en/research/free-resources/verification-and-validation/verification-tools.

Such a thickness would require an additional refinement of the surface and volumetric mesh to avoid high aspect ratio cells and possible simulation divergence.

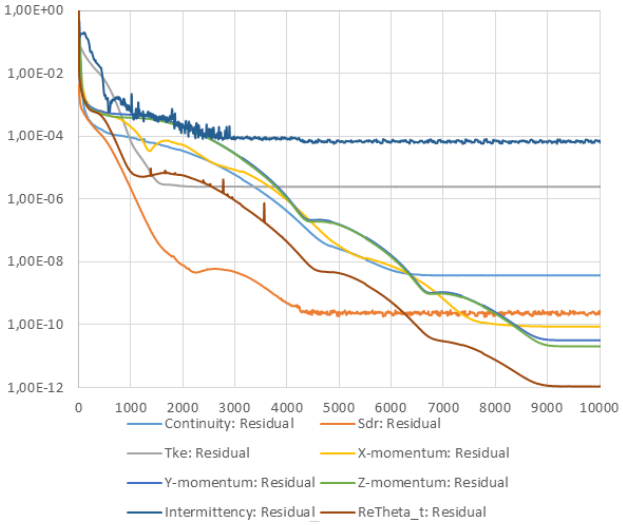

(a) P3590: MS+T residuals.

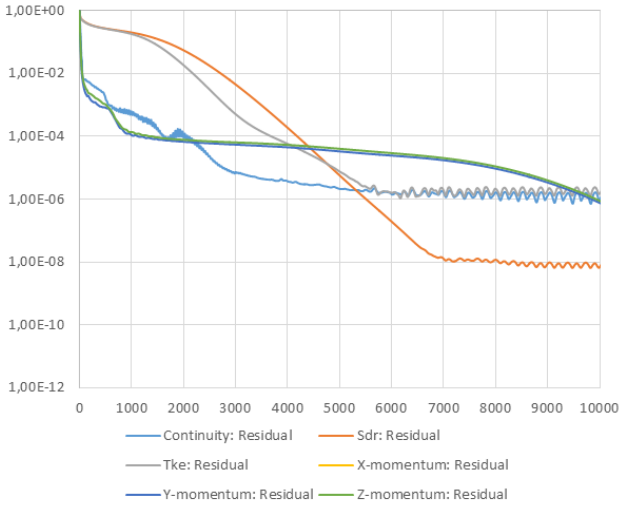

(b) P3590: FS residuals.

Figure 4: P3590: Residuals at $J = 0.788$ using $\gamma - Re_\theta$ in model scale (MS+T) and using $k-\omega$ SST in full scale (FS). Residuals are presented in L^2 norm and plotted in semi-logarithmic scale.

By comparing the predictions on the two meshes at the respective propeller's design condition (not shown here), it was observed that the wall treatment slightly affects the overall torque and thrust coefficient values in full-scale. The maximum relative difference of the predictions on the 'wall-resolved meshes', compared to the results obtained using wall functions, is within $\pm 0.5\%$ for both thrust and torque. This leads to a maximum relative difference in efficiency of 0.64%. This behavior is related to the fact that the pressure components are the major contributors to the overall thrust and torque, and they are minimally affected by the wall treatment. On the other hand, the wall treatment strongly affects the thrust and torque viscous components. The maximum relative difference of the results obtained on the 'wall-resolved' meshes with respect to those on the 'wall-function' meshes is approximately $\pm 7\%$. However, as the viscous contribution to the overall coefficients is less than 5%, the variation of the viscous components does not strongly affect the overall predictions. Following this comparison, it was judged that simulations using wall functions can accurately estimate the open water performance of a full-scale propeller. For this reason, 'wall-function' meshes are used in the following analysis. It is worth mentioning that, solely for this wall treatment comparison, simulations were run setting different inlet conditions than those reported in Table(4). Indeed, very high inlet eddy viscosity ratios would either cause the simulation to diverge or result in non-steady convergence on the 'wall-resolved' mesh.

The iterative convergence of the flow quantities using $\gamma - Re_\theta$ in model-scale and $k-\omega$ SST in full-scale is presented in Fig. 4 for propeller P3590 at $J = 0.788$. Residuals are plotted in norm L^2. The model-scale results refer to Grid 3 from Table 2. At this design condition, all the residuals fall below 10^{-6}, except for the intermittency γ residuals, that stagnate around 10^{-4}. This behavior of the intermittency residuals is well known. They are disturbed by the various limiters in the intermittency production term, as well as by the steady approximation of unsteady phenomena (see (Rubino 2021) for further details). The intermittency residuals also affect the turbulence kinetic energy (Tke) residuals' behavior since the production of TKE depends on the intermittency itself. Residuals of the flow quantities for the P1951 simulations behave similarly.

3.5 Inlet Conditions

No specific indication on the free-stream conditions were given in the experimental reports, and the unknown free-stream experimental conditions pose a limitation. Indeed, a rigorous validation exercise cannot be performed, since experimental conditions cannot be repeated with exactitude. To overcome this limitation, a sensitivity analysis, which is not shown here, was conducted to assess the influence of the turbulence intensity Tu at the propeller plane on the numerical results.

Tu at a specific position x^* is estimated from equation:

$$Tu = Tu_{in}\left(\left(1+\frac{3(x^*-x_{in})\beta Tu_{in}^2 U^* Re}{2(\mu^*_{t_{in}}/\mu)}\right)^{-\frac{\beta^*}{\beta}}\right)^{0.5}, \quad (7)$$

where $\beta = 0.0828$ and $\beta^* = 0.09$ are constants, U^* is the dimensionless initial velocity, x^* the dimensionless distance, and x_{in} is the distance to the inlet. Eq.(7) is obtained by the resolution of the $k-\omega$ SST transport equations for a uniform and steady flow, aligned with x, and neglecting the diffusion and cross-diffusion terms.

In the presented simulations, given the distance from the inlet, it is opted to add to the k and ω transport equations, Eq.(3) and Eq.(4), additional terms to counteract the k and ω destruction. These terms are equal to $-D_k$ for k equation and $-D_\omega$ for ω equation. They are active until a fixed distance x_d from the propeller plane, which is arbitrarily set to $0.3D$ in the present exercise. The values, imposed at the inlet $*_{in}$ and used in the simulations, are reported

in Table 4. These combinations of Tu_{in} and $\mu_{t_{in}}/\mu$ give a Tu value around 1% in the vicinity of the propeller plane. It is important to mention that these inlet turbulence intensities are chosen based on a qualitative comparison to measurements, rather than quantitative. Thus, the predictions of the limiting streamlines, as well as a smooth convergence of the residuals and forces, were prioritized over thrust and torque agreement with experiments.

The inlet conditions at full-scale were set to reproduce the same decay of the eddy viscosity ratio as in model-scale, following Baltazar et al. (2021). Nevertheless, it is worth pointing out that the inlet turbulence quantities do not affect the numerical solution when the flow is expected to be fully turbulent. The Reynolds number Re in Table 4 is defined as $Re = \frac{\rho c_{0.75R}\sqrt{U^2+(n\pi 0.75D)^2}}{\mu}$, where $U = JnD$ is the inlet velocity.

Table 4: Computations details: inlet and initial conditions.

	Re	n	$Tu_{in}(\%)$	$\mu_{t_{in}}/\mu$
P3590 MS	7.32×10^5	19 Hz	1%	10
P3590 FS	6.29×10^7	1.27 Hz	1%	858
P1951 MS	9.98×10^5	24 Hz	2%	10
P1951 FS	1.48×10^7	4.68 Hz	2%	150

4 RESULTS

4.1 Open Water Curves (OWC)

The open water curves for both propellers are presented in Fig. 5. In all computations, n is kept constant, while the inlet velocity U is varied with respect to the considered advance coefficient J. Predictions in model-$_{MS}$ and full-scale $_{FS}$ are compared to the experimental results $_{exp}$ provided by SVA and HSVA and to the extrapolated-to-full-scale values $_{explt}$ obtained using the 1978 ITTC method for the P1951 and Streckwalll's strip method for the P3590. The efficiency is defined as $\eta = JK_T/(2\pi K_Q)$. Open water curves for P3590 are shown in Fig. 5a. There is a good agreement between the thrust and torque coefficients predictions in model-scale and the measurements.

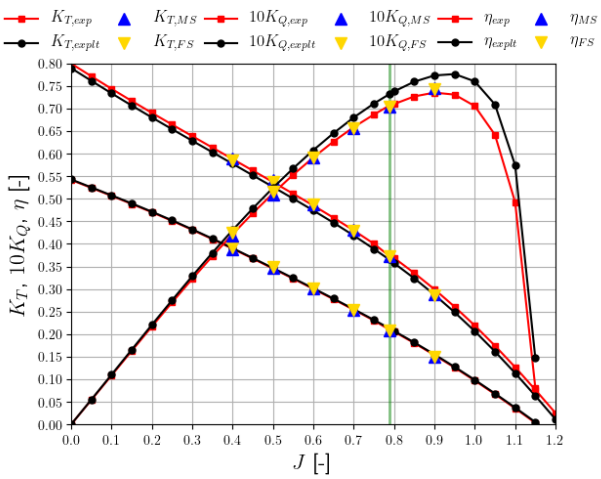

(a) P3590: OWC.

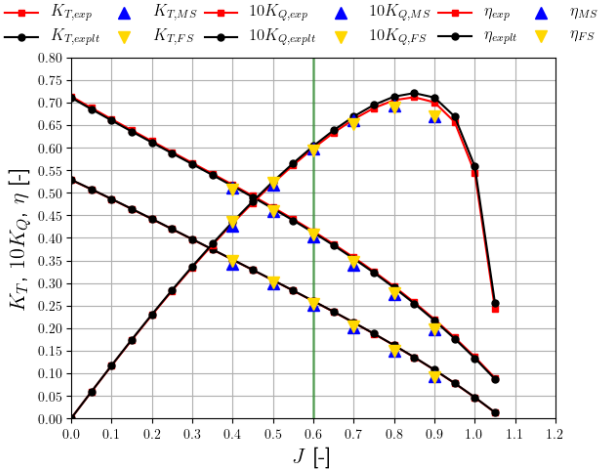

(b) P1951: OWC.

Figure 5: P3590 and P1951 open water curves in model- and full-scale. Predictions in model-scale are validated against the experimental data provided by SVA and HSVA, while in full-scale against the coefficients extrapolated using the 1978 ITTC method for the P1951 and the strip method by Streckwall for the P3590. Data are labeled as: model-scale predictions $K_{T,MS}$, $10K_{Q,MS}$, η_{MS}; full-scale predictions $K_{T,FS}$, $10K_{Q,FS}$, η_{FS}; experiments $K_{T,exp}$, $10K_{Q,exp}$, η_{exp}; extrapolated-to-full-scale values $K_{T,explt}$, $10K_{Q,explt}$, η_{explt}. The green line corresponds to the J at design condition: $J = 0.788$ for P3590, $J = 0.6$ for P1951.

The relative deviation from the experimental thrust coefficient is below 0.56%, and below 0.7% for the torque coefficient at all relevant loading conditions. This results in a relative deviation from the experimental efficiency η_{exp} below 1.3% at all J. It can be noticed that the predicted scale effects are very small, whereas the extrapolated efficiency values, η_{explt}, using the Streckwall's strip method, are considerably higher than predictions. For instance, η_{explt} is 3.82% higher than η_{FS} at the design condition $J = 0.788$. This deviation results from the higher predicted values of torque coefficient and lower predicted values of thrust coefficient, when compared to the extrapolated quantities. Open water curves for the P1951 are shown in Fig. 5b. In general, the efficiency in model-scale, η_{MS}, is under-predicted at all loading conditions. The efficiency relative deviation from the measurements is below 1% for $0.5 \leq J \leq 0.7$, but it becomes more important at the extremities of the studied J range, reaching 1.77% at $J = 0.8$. The under-prediction of efficiency is related to the more important thrust under-prediction than torque. $K_{T,MS}$ relative deviation from $K_{T,exp}$ has a minimum 2.3% at $J = 0.6$ and it is equal to 7% at $J = 0.8$. On the other hand, $K_{Q,MS}$ relative deviation from $K_{Q,exp}$ increases from 1.26% at $J = 0.4$ to 6% at $J = 0.8$. When compared to full-scale, the predicted scale effects are small at all loading conditions. The same conclusion is drawn if the full-scale results, as extrapolated using the 1978 ITTC method, are compared to measurements. Nevertheless, full-scale efficiency predictions η_{FS} are

lower than the extrapolated values η_{explt}, as it is clearly visible at the lightest loading conditions. This behavior is related to the fact that the predicted $K_{T,FS}$ is considerably lower than the extrapolated value $K_{T,explt}$, i.e. the deviation is around 8% at $J = 0.8$. To better understand the flow physics, it is decided to analyze the surface flow at the propellers' design conditions.

4.2 P3590 at J=0.788

In Fig. 6, the experimental paint streaks on the P3590 pressure and suction sides are shown for $J = 0.788$. The laminar and turbulent flow regimes are clearly distinguishable from the streamlines direction. In a laminar flow regime, the streamlines are more radially directed, because of the dominance of the centrifugal force. Whereas, in a turbulent boundary layer, the turbulent shear stresses become more important, and the paint streaks are more chordwise directed (Kuiper 1971). At this loading condition, the flow regime on both sides of the propeller is mainly laminar. On the suction side, an important laminar separation can be observed all along the propeller trailing edge. On the pressure side, the change in the streamlines directions indicate flow transition close to the propeller's tip trailing edge. The numerical results, as obtained on Grid 3, are shown in Fig. 7. The limiting streamlines are presented over the skin friction contours, with $C_f = 2\tau_w/\rho U^2$. Limiting streamlines predictions are in good agreement with measurements. The trailing edge laminar separation is well predicted on the suction side, see Fig. 7b. With the help of the skin friction contours, the flow transition at the tip on the suction side and before separation can be observed. On the other hand, the flow remains mainly laminar on the pressure side, Fig. 7a. An indication of flow transition is visible at the tip trailing edge, while laminar flow separation is visible at lower radii. When comparing predictions by $\gamma - Re_\theta$ with predictions by $k-\omega$ SST in Fig. 7a and Fig. 7c, it is clear that a transition model is essential to predict the right flow features. A turbulence model alone is not able to predict any laminar separation along the trailing edge on the suction side, but rather a turbulent separation occurring at lower radii, see Fig. 7d.

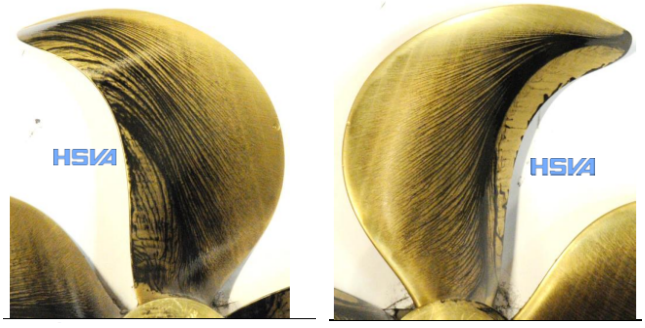

(a) P3590: PS (EXP). (b) P3590: SS (EXP).

Figure 6: P3590: Experimental paint streaks, as measured by HSVA in their towing tank, on the pressure (PS) and on the suction side (SS), at the design condition $J = 0.788$.

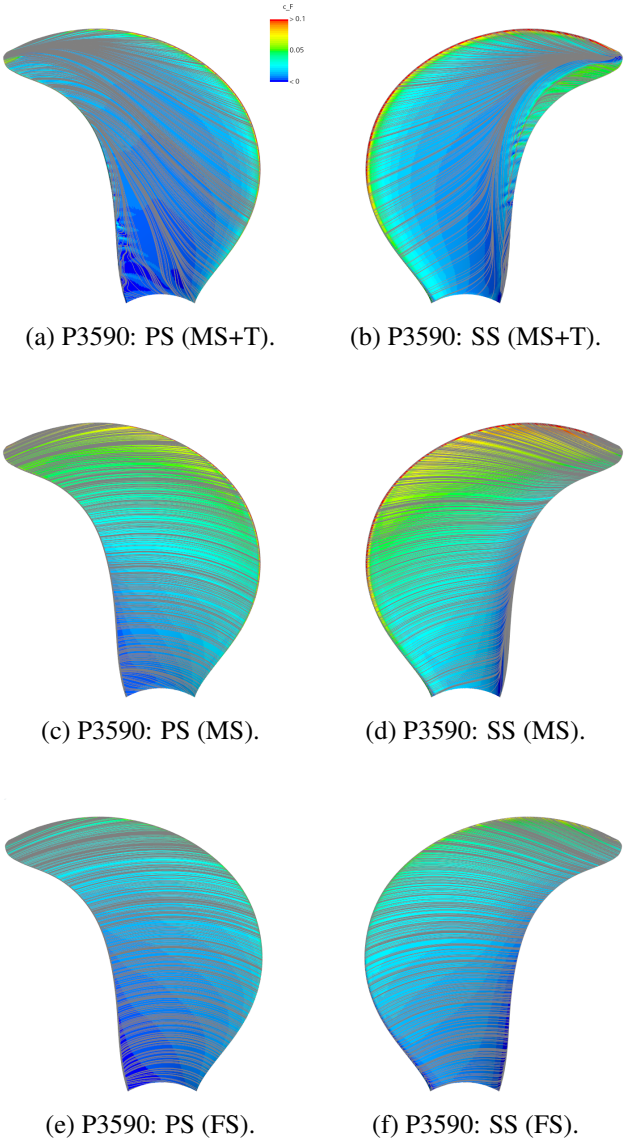

(a) P3590: PS (MS+T). (b) P3590: SS (MS+T).

(c) P3590: PS (MS). (d) P3590: SS (MS).

(e) P3590: PS (FS). (f) P3590: SS (FS).

Figure 7: P3590: Predictions in model-scale with (MS+T) and without (MS) transition model and in full-scale (FS) at the design condition $J = 0.788$. Wall streamlines are plotted over skin friction, $C_f = 2\tau_w/\rho U^2$, contours on both the pressure (PS) and suction (SS) sides.

In conclusion, the flow predicted by $k-\omega$ SST in model-scale appears mainly turbulent on both propeller surfaces. The limiting streamlines in full-scale are presented in Fig. 7f and Fig. 7e. It can be observed that they are chordwise-directed, indicating a fully turbulent flow at all radii.

In Fig. 8, the skin-friction C_f and the pressure coefficient $-C_p = -2(P-P_\infty)/\rho(U^2+(n\pi 0.75D)^2)$ distributions at $r = 0.75R$ are presented. Model-scale predictions using $\gamma - Re_\theta$ are compared to full-scale predictions using $k-\omega$ SST. At this section, the $-C_p$ distribution is slightly higher in full-scale all along the blade profile at both sides. The main difference occurs between $0.8 < s/c < 0.95$, because of the laminar separation in model-scale, as indicated by the $-C_p$ plateau in Fig. 8a. The C_f distribution is shown in

Table 5: P3590: Thrust and torque coefficients and efficiency for the design condition $J = 0.788$ on Grid 3. Model- and full-scale predictions are presented alongside the measured values and the extrapolated values using the Streckwall's strip method ($FS_{Streckwall}$). The percentages indicate the relative deviation of model-scale predictions from the measurements.

	EXP	MS	MS+T	$FS_{Streckwall}$	FS
$10K_Q$	0.3733	0.3697(-0.95%)	0.3729(-0.11%)	0.3652	0.3719
$10K_{Q,p}$		0.3307	0.3563		0.3515
$10K_{Q,n}$		0.0390	0.0166		0.0204
K_T	0.2102	0.1933(-8%)	0.2094(-0.38%)	0.2130	0.2086
$K_{T,p}$		0.1981	0.2111		0.2112
$K_{T,n}$		-0.0048	-0.0017		-0.0026
η	0.7061	0.6557 (−7.14%)	0.7043 (−0.25%)	0.7314	0.7035

Fig. 8b and it is noticed that scale effects on skin friction are more important than for the pressure.

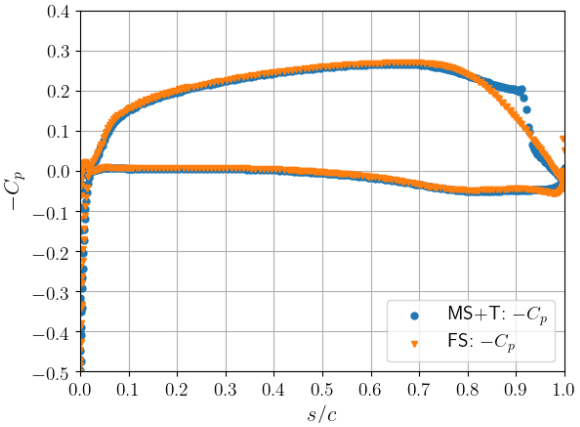

(a) P3590: $-C_P$.

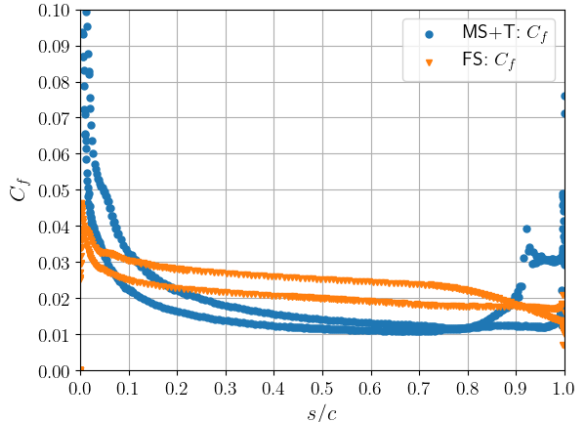

(b) P3590: C_f.

Figure 8: P3590: skin friction C_f and pressure coefficient $-C_p$ distributions at $r = 0.75R$ for the design condition $J = 0.788$. Model-scale predictions using $\gamma - Re_\theta$ (MS+T) are compared to full-scale predictions using $k-\omega$ SST (FS).

The thrust and torque coefficients, and efficiency, at all scales and as predicted by the different models, are reported in Table 5. Measured and extrapolated-to-full-scale values are presented as well. A closer agreement of K_T and $10K_Q$ with respect to the experiments is evident when the transition model is used. In particular, K_T relative deviation from measurements is reduced from 8% to 0.38%.

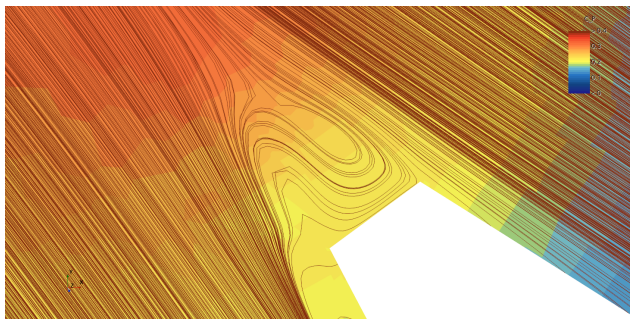

(a) P3590: MS+T.

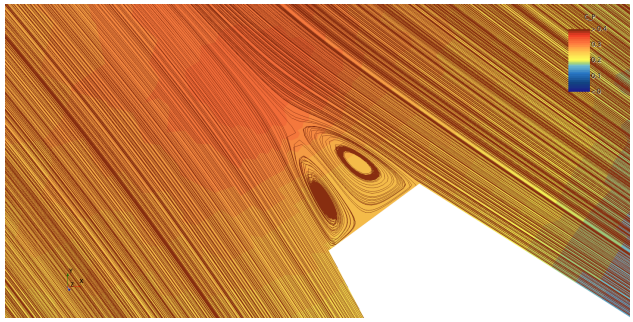

(b) P3590: FS.

Figure 9: P3590: Plane section z/R=0.5. Visualization of the recirculation zone behind the propeller trailing edge in full- and model-scale at the design condition J=0.788. Streamlines are plotted on the pressure coefficient contours, where $C_p = 2(P - P_\infty)/\rho(U^2 + (n\pi 0.5D)^2)$.

In terms of torque predictions in model-scale, the use of the transition model is less obvious. The laminar separation leads to a higher pressure torque component and a lower viscous torque one, but the overall torque is very close to the torque obtained in a fully turbulent simulation. Focusing on the predicted scale effects for the P3590 at this particular operating condition, the increase of Reynolds number leads to a decrease in $10K_Q$, as well as in K_T, with respect to the predictions by $\gamma - Re_\theta$. The decrease in torque comes from its pressure component. It

is mainly due to the different boundary layer flows and, to a lesser extent, it is also related the higher pressure exercised by the trailing edge vortices on the blunt trailing edge, see Fig. 9a vs Fig. 9b. For what concerns the predicted K_T, its pressure component slightly increases from model- to full-scale because of the larger separation area behind the trailing edge in model-scale. Nevertheless, its viscous component decreases in full-scale. A more detailed analysis of the shear thrust coefficient, $K_{t,n}$, radial distributions in model- and full-scale showed that the largest differences are concentrated in the interval $0.8 < r/R < 0.9$. This corresponds to the region where the blade starts approximately to be raked towards the suction side. However, a precise evaluation of the viscous component of the thrust and torque coefficients is complicated to conduct. Indeed, the viscous components strongly depend on the wall treatment and the inlet conditions. For instance, it is unquestionable that a slightly different tuning of the inlet turbulence intensity and eddy viscosity ratio would mainly change the viscous components of the forces. Indeed, both γ and Re_{θ_t} production terms depend on the free-stream turbulence intensity. A study of the effect of the inlet turbulence intensity on the forces demonstrated that in a range of Tu_{in} between 0.5% and 1.5%, for fixed eddy viscosity ratios, the viscous components of the forces can vary up to a maximum of $\pm 11\%$ in $K_{T,n}$ and $\pm 8\%$ in $K_{Q,n}$ with respect to the forces obtained using $Tu_{in} = 1\%$ (Table 5), without considerably changing the flow physics. On the other hand, the pressure component variations remain within $\pm 1\%$. As the viscous components of the thrust and torque contribute minimally to the overall forces, slightly different inlet conditions would not change the overall scenario and the predicted scale effects on this propeller would still be small. It is worth noticing that the predicted scale effects would be greater if the force coefficients calculated by $k-\omega$ SST were considered instead of those obtained with $\gamma - Re_\theta$ in model-scale. The efficiency at full-scale would be 7% higher than at model-scale, because of the higher thrust coefficient. The latter is due to the smaller separation area in full-scale. Numerical predictions are not in agreement with the values extrapolated using the strip method by Streckwall, for which it is obtained an η_{extpl} 3.6% higher than η_{exp}. The discrepancy between the simulation and extrapolation results is due to the different values of the thrust, $K_{T,extpl}$ is 2% higher than $K_{T,FS}$, and the torque coefficients, $K_{Q,extpl}$ is 3.7% smaller than $K_{Q,FS}$. These deviations are due to the fact that the blunt trailing edge is not considered in the extrapolation. For example, it is known that sharpening a blunt trailing edge leads to a significant increase in the thrust coefficient (see for example Brown et al. 2014).

4.3 P1951 at J=0.6

The experimental and numerical results for the propeller P1951 are shown in Fig. 10 and Fig. 11, respectively. Predictions obtained by $\gamma - Re_\theta$ in model-scale are presented alongside the results obtained using $k-\omega$ SST in model- and full-scale. If transition results, Fig. 11a and Fig. 11b, are compared to the experimental results presented in Fig.10, a good agreement is noticed between predictions and measurements.

(a) P1951: PS (EXP). (b) P1951: SS (EXP).

Figure 10: P1951: Experimental paint streaks, as measured by SVA in their towing tank, on the pressure (PS) and on the suction side (SS), at the design condition $J = 0.6$.

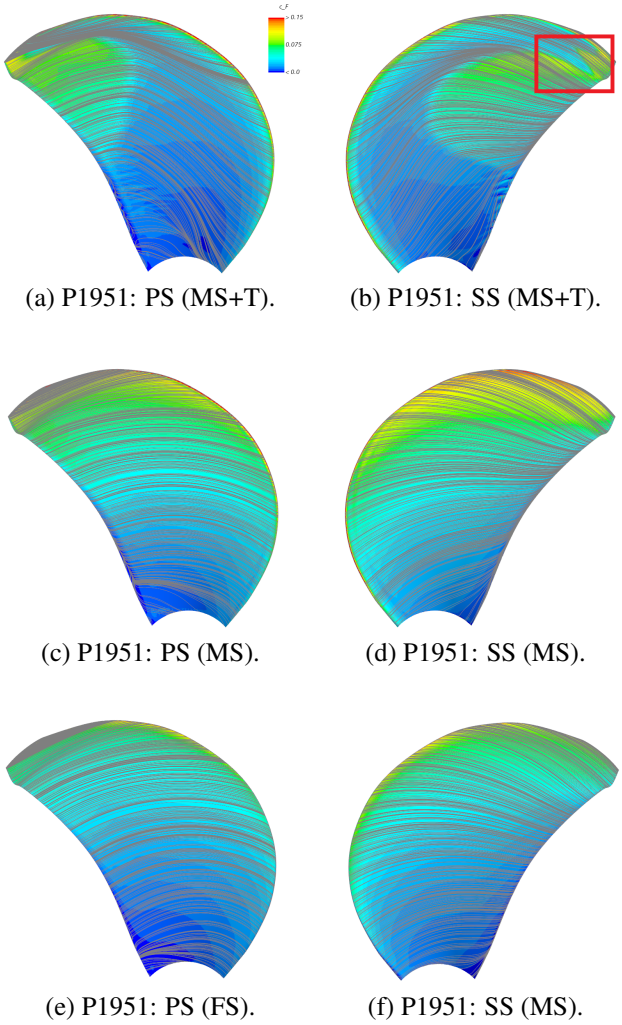

(a) P1951: PS (MS+T). (b) P1951: SS (MS+T).

(c) P1951: PS (MS). (d) P1951: SS (MS).

(e) P1951: PS (FS). (f) P1951: SS (MS).

Figure 11: P1951: Numerical prediction in model scale with (MS+T) and without (MS) transition model- and in full-scale (FS) at the design condition $J = 0.6$. Wall streamlines are plotted over skin friction contours plotted over skin friction, $C_f = 2\tau_w/\rho U^2$, contours on both the pressure (PS) and suction (SS) sides.

Taken the streamlines as a reference, the flow on the suction side starts its transition at radii $r < 0.5R$, as in the experiments, and it appears turbulent towards the trailing edge of the raked tip. Nevertheless, numerically, a laminar spike is visible in the skin friction distribution, in correspondence of the radius where the surface is raked towards the pressure side (red rectangle in Fig. 11b). Its existence cannot be proven in the experiments. Nevertheless, it is probable that some crossflow may occur in this region. Indeed, the surface curvature and the mild favorable pressure gradient in that region may cause the development of the unstable crossflow velocity component in the boundary layer. On the pressure side, the agreement is slightly off, Fig. 10a vs Fig. 11a. As predicted by $\gamma - Re_\theta$, the turbulence flow region is wider on the upper half of the propeller blade, i.e. for $r/R > 0.5$, while the flow stays laminar closer to the hub intersection. However in the experiments the turbulence region is uniform at all radii, starting from half of the propeller chord. Contrary to the results by $\gamma - Re_\theta$, $k-\omega$ SST fails to predict the laminar flow, since the flow appears turbulent right after the leading edge, Fig. 11c and Fig. 11d. Finally, Fig. 11e and Fig. 11f present the results in full-scale, that show a fully turbulent flow on both surfaces.

$-C_p$ and C_f distributions at $r/R = 0.75$ are presented in Fig. 12. Differences between model- and full-scale predictions are less obvious for the pressure coefficient distribution compared to the previous propeller, see Fig. 12a. Nevertheless, it can be observed that $-C_p$ in model-scale is slightly higher when compared to the full-scale values all along the chord direction. The two pressure coefficient distributions do not differ qualitatively, and scale effects on the pressure are rather small. Results for the C_f distribution are shown in Fig. 12b. A laminar-to-turbulent C_f distribution in model scale is clearly distinguishable from the fully turbulent C_f distribution in full-scale. In the first case, the chord position at which the flow starts transitioning can be identified as the s/c coordinates at which the C_f starts increasing. This position corresponds to $s/c \sim 0.35$ on the suction side, and to $s/c \sim 0.55$ on the pressure side.

The forces coefficients are presented in Table 6. The use of $\gamma - Re_\theta$ improves considerably the K_T results, reducing the relative deviation from the measured value from 5% to 2.96%. On the other hand, deviation in $10K_Q$ increases in $\gamma - Re_\theta$ results with respect to $k-\omega$ SST predictions in model-scale. The reason might be related to the under-prediction of turbulence on the pressure side when using the transition model.

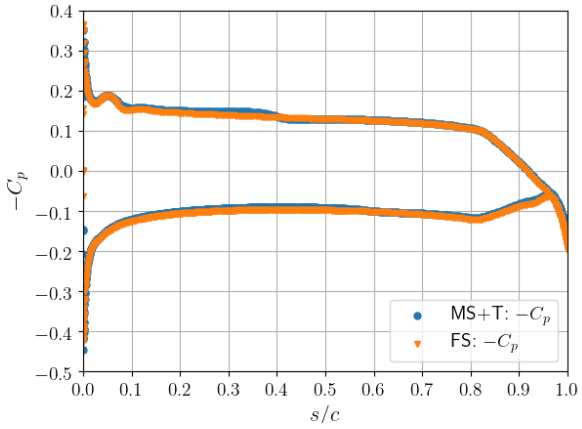

(a) P1951: $-C_P$.

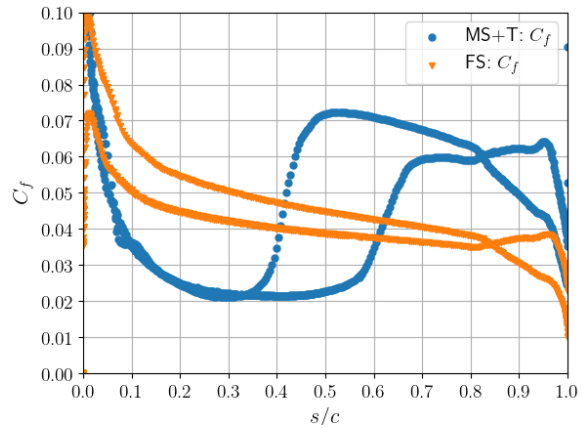

(b) P1951: C_f.

Figure 12: P1951: skin-friction C_f and pressure coefficient $-C_p$ distributions at $r = 0.75R$ for the design condition $J = 0.6$. Model scale predictions using $\gamma - Re_\theta$ (MS+T) are compared to full-scale predictions using $k-\omega$ SST (FS).

Table 6: P1951: Thrust and torque coefficients, and efficiency for the design condition $J = 0.6$ on Grid 2. Model- and full-scale predictions are presented alongside the measured values and the extrapolated values using the ITTC 1978 method ($FS_{ITTC1978}$). The percentages indicate the relative deviation of model scale predictions from the measurements.

	EXP	MS	MS+T	$FS_{ITTC\ 1978}$	FS
$10K_Q$	0.4145	0.4145 ($\sim 0\%$)	0.4028(-2.8%)	0.4117	0.4068
$10K_{Q,p}$		0.3703	0.3751		0.3764
$10K_{Q,n}$		0.0442	0.0277		0.0304
K_T	0.2598	0.2468 (-5%)	0.2521 (-2.96%)	0.2601	0.2532
$K_{T,p}$		0.2519	0.2554		0.2566
$K_{T,n}$		-0.0051	-0.0035		-0.0034
η	0.5986	0.5685 (-5%)	0.5977(-0.15%)	0.6034	0.5943

If the results in model-scale are compared to full-scale predictions, it can be observed that the predicted scale effects are very small. Indeed, the predicted increase in thrust in full-scale is counterbalanced by the increase in torque, due to its pressure component.

As in the simulations, the same trend in scale effects is observed for the extrapolated values, obtained using the 1978 ITTC method, with respect to the measurements. The extrapolated scale effects on K_T and K_Q are rather small. Nevertheless, efficiency predictions deviate quantitatively from the extrapolated values. Using the ITTC 1978 procedure a decrease in torque is estimated, which is not observed numerically. As for the previous propeller, it is important to notice that this would not be the case if predictions at full-scale were compared to predictions in model-scale without transition model.

It is worth mentioning that the ITTC 1978 extrapolation procedure accounts for surface roughness, $k = 1.5e^{-5}m$ for the present case, which is neglected in the presented computations. The inclusion of roughness is expected to affect qualitatively the numerical results. Nevertheless, when roughness is numerically included, predictions of thrust and torque coefficients are expected to be lower than the case of a smooth blade. For this reason, despite the possible important quantitative variations, the authors do not expect significant differences in the predicted trends for the propeller's efficiency when the roughness is included. Further simulations are needed to prove this hypothesis.

5 CONCLUSIONS

The scale effects on two different unconventional propellers, P3590 and P1951, were analyzed in terms of hydrodynamic performance characteristics, skin friction contours, and limiting streamlines. Results in model-scale were computed using the transition model $\gamma - Re_\theta$, which was proven to be essential to predict the correct flow physics. Indeed, at the lowest Reynolds number, the flow is mainly laminar, and a turbulence model predicts a fully turbulent flow. When model-scale numerical results by $\gamma - Re_\theta$ were compared to full-scale predictions by $k-\omega$ SST, it was found that scale effects are negligible for both propellers in terms of hydrodynamic performance. Indeed, an increase in thrust is counterbalanced by an increase in torque, or vice versa, leading to similar values of efficiency at the different Reynolds numbers. This behavior stands in contrast with the results obtained when using $k-\omega$ SST for both model- and full-scale predictions. Indeed, the turbulence model predicts significant scale effects on the thrust coefficient. The results for P1951 were qualitatively, but not quantitatively, in agreement with the extrapolated-to-full-scale values obtained using the 1978 ITTC method. On the other hand, P3590 predictions in full-scale considerably differed from the extrapolated values obtained using Streckwall's strip method. These discrepancies come from the fact that the extrapolation method does not account for the blunt trailing edge of the propeller blade. The latter plays an important role in the formation of trailing edge vortices, affecting the propeller performance coefficients at full-scale. Future works will include a mesh convergence study in full-scale to assess numerical uncertainties, and new simulations, including wall roughness with wall functions, to further confirm the trends observed in this work.

ACKNOWLEDGMENTS

The authors thank the Federal Ministry for Economic Affairs and Climate Action (BMWK) and Projektträger Jülich (PTJ) for funding this work through the PropTiForm project. This work was carried out within the framework of the research project DEffProForm in cooperation with FRIENDSHIP SYSTEMS AG, HSVA GmbH, ISA Propulsion GmbH & Co. KG, Mecklenburger Metallguss GmbH, SVA Potsdam GmbH, and the Institute for General Electrical Engineering at the University of Rostock. A special acknowledgment to HSVA and SVA for providing the propeller geometries and the experimental data to compare our simulations with.

REFERENCES

Baltazar, J., Rijpkema, D., & Falcão de Campos, J. (2021). 'Prediction of the propeller performance at different Reynolds number regimes with RANS'. Journal of Marine Science and Engineering, **9**(10), pp. 1115.

Bhattacharyya, A., Krasilnikov, V., & Steen, S. (2016). 'Scale effects on open water characteristics of a controllable pitch propeller working within different duct designs'. Ocean Engineering, **112**, pp. 226-242.

Brown, M., Sánchez-Caja, A., Adalid, J. G., Black, S., Sobrino, M. P., Duerr, P.,& Saisto, I. (2014). 'Improving propeller efficiency through tip loading'. In 30th Symposium on Naval Hydrodynamics Hobart.

Choi, J. K., & Kim, H. T. (2020). 'An investigation on the effect of the wall treatments in RANS simulations of model and full-scale marine propeller flows'. International Journal of Naval Architecture and Ocean Engineering,**12**, pp. 967-987.

Eça, L. & Hoekstra, M. (2014). 'A procedure for the estimation of the numerical uncertainty of CFD calculations based on grid refinement studies'. Journal of Computational Physics, **262**, pp 104-130.

Helma, S., Streckwall, H., & Richter, J. (2018). 'The effect of propeller scaling methodology on the performance prediction'. Journal of Marine Science and Engineering, **6**(2).

ITTC (1978). '1978 ITTC performance prediction method'. ITTC-Recommended Procedures and Guidelines, ITTC Zürich, Switzerland.

ITTC Propulsion Committee (2014, August). 'Final report and recommendations to the 27th ITTC. In Proceedings of the 27th International Towing Tank Conference, Copenhagen, Denmark.

ITTC Propulsion Committee (2017, September). 'Final report and recommendations to the 28th ITTC. In Proceedings of the 28th International Towing Tank

Conference, Wuxi, China.

Krasilnikov, V., Sun, J., & Halse, K. H. (2009, June). 'CFD investigation in scale effect on propellers with different magnitude of skew in turbulent flow'. In the First International Symposium on Marine Propulsors, Trondheim, Norway.

Kuiper, G. (1981). ' Cavitation inception on ship propeller models'. Doctoral dissertation, Delft University of Technology.

Langtry, R. B. (2006). 'A correlation-based transition model using local variables for unstructured parallelized CFD codes'. Doctoral dissertation, University of Stuttgart.

Li, D. Q., Lindell, P., & Werner, S. (2019). Transitional flow on model propellers and their influence on relative rotative efficiency. Journal of Marine Science and Engineering, 7(12), 427.

Menter, F. R., (1994). Two-Equation Eddy-Viscosity Turbulence Models for Engineering Applications. AIAA Journal,32(8) pp. 1598-1605.

Müller, S. B., Abdel-Maksoud, M., & Hilbert, G. (2009, June). 'Scale effects on propellers for large container vessels'. In the First International Symposium on Marine Propulsors, Trondheim, Norway.

Pawar, S., & Brizzolara, S. (2019). 'Relevance of transition turbulent model for hydrodynamic characteristics of low Reynolds number propeller'. Applied Ocean Research, **87**, pp. 165-178.

Rubino, G. (2021). 'Laminar-to-turbulence Transition Modeling of Incompressible Flows in a RANS Framework for 2D and 3D Configurations'. Doctoral dissertation, École centrale de Nantes.

Sánchez-Caja, A., González-Adalid, J., Pérez-Sobrino, M., & Sipilä, T. (2014). 'Scale effects on tip loaded propeller performance using a RANSE solver'. Ocean Engineering, **88**, pp. 607-617.

Shin, K. W., & Andersen, P. (2017, June). 'CFD analysis of scale effects on conventional and tip-modified propellers'. In Fifth International Symposium on Marine Propulsors, Espoo, Finland.

Streckwall, H., Greitsch, L., Müller, J., Scharf, M., & Bugalski, T. (2013). 'Development of a strip method proposed as new standard for propeller performance scaling'. Ship Technology Research, **60**(2), pp. 58-69.

Yao, H., & Zhang, H. (2018). 'Numerical simulation of boundary-layer transition flow of a model propeller and the full-scale propeller for studying scale effects'. Journal of Marine Science and Technology, **23**, pp. 1004-1018.